

Determination of the neutrino fluxes in the Brookhaven wide-band beams

L. A. Ahrens, S. H. Aronson, P. L. Connolly,* B. G. Gibbard, M. J. Murtagh, S. J. Murtagh,[†]
S. Terada, and D. H. White

Physics Department, Brookhaven National Laboratory, Upton, New York 11973

J. L. Callas, D. Cutts, M. Diwan, J. S. Hoftun, R. E. Lanou, and T. Shinkawa[‡]

Department of Physics, Brown University, Providence, Rhode Island 02912

Y. Kurihara

Department of Physics, Hiroshima University, Hiroshima 730, Japan

K. Amako and S. Kabe

National Laboratory for High Energy Physics (KEK), Ibaraki-ken 305, Japan

Y. Nagashima, Y. Suzuki, S. Tatsumi, and Y. Yamaguchi

Physics Department, Osaka University, Toyonaka, Osaka 560, Japan

K. Abe,[‡] E. W. Beier, D. C. Doughty,[§] L. S. Durkin, S. M. Heagy, M. Hurley,
A. K. Mann, F. M. Newcomer, H. H. Williams, and T. York**

Department of Physics, University of Pennsylvania, Philadelphia, Pennsylvania 19104

D. Hedin, M. D. Marx, and E. Stern

Department of Physics, State University of New York at Stony Brook, Stony Brook, New York 11794

(Received 17 January 1986)

The neutrino fluxes $\phi(E(\nu_\mu))$, $\phi(E(\bar{\nu}_\mu))$, and $\phi(E(\nu_e))$ in the Brookhaven Alternating Gradient Synchrotron wide-band beams have been determined by measurements of quasielastic interactions observed in a massive, high-resolution detector. These fluxes are accurately reproduced by Monte Carlo calculations.

I. INTRODUCTION

A primary goal of recent neutrino experiments^{1,2} at the Brookhaven Alternating Gradient Synchrotron (AGS) has been the measurement of the absolute cross sections for the weak neutral-current reactions

$$\nu_\mu e \rightarrow \nu_\mu e, \quad (1)$$

$$\bar{\nu}_\mu e \rightarrow \bar{\nu}_\mu e, \quad (2)$$

$$\nu_\mu p \rightarrow \nu_\mu p, \quad (3)$$

$$\bar{\nu}_\mu p \rightarrow \bar{\nu}_\mu p. \quad (4)$$

To obtain the integrated neutrino flux necessary for absolute normalization of the cross sections of reactions (1)–(4), data on the following theoretically and experimentally well-understood weak charged-current quasielastic reactions were acquired at the same time³ to supplement earlier measurements:⁴

$$\nu_\mu n \rightarrow \mu^- p, \quad (5)$$

$$\bar{\nu}_\mu p \rightarrow \mu^+ n. \quad (6)$$

In addition, data were obtained for the $\nu_e n$ quasielastic interaction

$$\nu_e n \rightarrow e^- p. \quad (7)$$

These quasielastic reactions are used to determine the neutrino fluxes $\phi(E(\nu_\mu))$, $\phi(E(\bar{\nu}_\mu))$, and $\phi(E(\nu_e))$. Knowledge of the flux shapes as a function of neutrino energy is necessary to analyze the data from the neutral-current reactions, including corrections for the relative composition of ν_μ , $\bar{\nu}_\mu$, and ν_e in each beam.

This paper presents measurements of the neutrino fluxes in both the primarily ν_μ and primarily $\bar{\nu}_\mu$ wide-band beams at the Brookhaven AGS. The rates of reactions (5) and (6) determine $\phi(E(\nu_\mu))$ and $\phi(E(\bar{\nu}_\mu))$, respectively, and also the relative composition of $\bar{\nu}_\mu$ and ν_μ in each beam as a function of neutrino energy. The flux $\phi(E(\nu_e))$ in the primarily ν_μ beam is measured by reaction (7). The measured fluxes are compared to fluxes from a Monte Carlo calculation which is described in this paper.

Sections II and III discuss the components of the neutrino beam line and certain aspects of the sources of various neutrino types. Section IV briefly describes the detector in which the neutrino-induced events were observed and measured. Section V discusses the flux measurements and presents the measured spectra. In Sec. VI the Monte Carlo neutrino flux calculation is described and the calculated neutrino spectra are compared with the observed spectra.

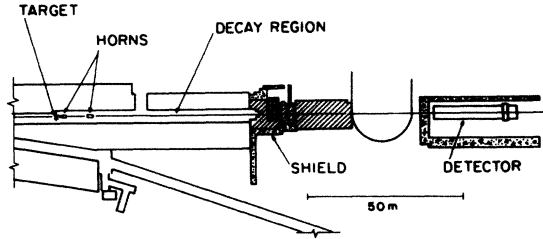


FIG. 1. The wide-band neutrino beam line and decay region are shown with the magnetic horns and the detector.

II. THE BEAM LINE

To produce the wide-band neutrino beam, protons are accelerated to an energy of 28.3 GeV in the Brookhaven AGS. The proton beam is extracted in a single revolution⁵ and transported to a target as shown in Fig. 1. The full width of the circular beam at the target is 2 mm. The time structure of the beam is preserved during the extraction process so that the proton beam arrives at the target in 12 bunches 224 ns apart; the width of each bunch is about 30 ns. The corresponding neutrino-beam time structure, measured with neutrino interactions, is shown in Fig. 2.

Secondary particles of selected sign which originate from collisions of protons in the target are focused in the toroidal magnetic fields produced by a system of axially symmetric current carrying elements (horns) shown schematically in Fig. 3. The target, embedded in the front of horn 1, is sapphire (Al_2O_3) 6.4 mm in diameter, 45 cm long, and represents about two interaction lengths. The charged particles produced in the target are reduced in angular spread by each of the two horns. The result is a nearly parallel beam in the decay region. It is desirable to provide high transmission over as wide a momentum range as possible, hence the shape of the horns is tailored to optimize the collection efficiency at the most probable angle for particle production at each momentum.⁶ In this design, the low-momentum particles cross over between

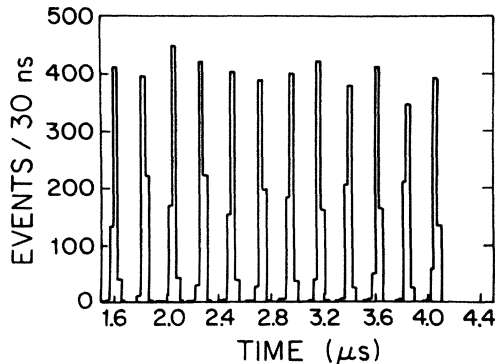


FIG. 2. The AGS has 12 proton bunches circulating, and extraction is accomplished in a single revolution. The time structure of the proton beam is preserved through extraction and transport to the target; the bunch structure is shown here as measured by charged-current neutrino interactions in the detector.

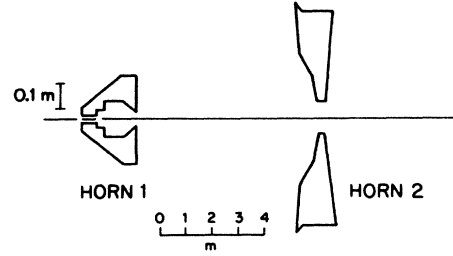


FIG. 3. The magnetic horn system is shown schematically. The horns themselves are cylindrically symmetric, with the proton target enclosed in the entrance to the first horn.

the two horns, but at higher momentum the divergence of the particles is simply reduced at each horn.

A simplified schematic diagram for the horn-current power supply is shown in Fig. 4. The energy-storage capacitors C are charged at constant current to about 12 kV in the 1.4 s between AGS pulses. The capacitors are arranged in 20 modules, each $42 \mu\text{F}$, and the modules are switched on to the load through ignitrons. After triggering, the system behaves as a series RLC circuit with a time constant of $32 \mu\text{s}$. The ignitrons and the kicker magnet which is used to extract the proton beam from the AGS are both triggered by a pulse synchronized to the AGS radio-frequency accelerating field; hence the horn trigger is stable with respect to beam time to a few ns. The actual time variation between horn current and beam is set by jitter inherent to the ignitrons which is observed to be of order $0.1 \mu\text{s}$, and hence negligible given the $32\text{-}\mu\text{s}$ time constant of the system. The current pulse is shown in Fig. 5. At the time when the beam is present the current is 250 kA. The current is monitored absolutely in one module of the power supply, and in a relative sense in the system as a whole. The time required to charge the capacitor bank from the constant current source indicates how many of the 20 modules have properly discharged on the previous cycle, and hence is a useful parameter to monitor.

In the shield at the end of the decay region are ion chambers which monitor the muon flux. These chambers can be moved in either a vertical or horizontal direction and are used to monitor the beam alignment and intensity.

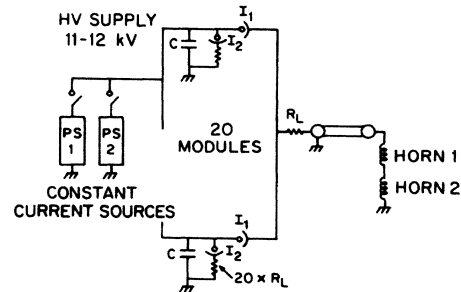


FIG. 4. The power supply to the horn is shown in schematic form. The supply consists of 20 modules, two of which are shown.

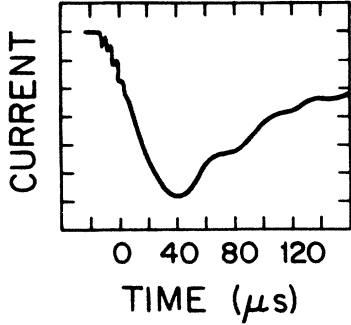


FIG. 5. The current pulse in the horn system, the peak current was measured at 250 kA and the sweep speed is 20 μ s per cm.

III. NEUTRINO SOURCES

Charged π and K mesons produced in the target yield neutrinos through their decay. The muon neutrinos from K decay contribute significantly only at the high-momentum end of the spectrum.

The predominant branching mode of the π meson is $\pi \rightarrow \mu \nu_\mu$, and for neutrinos close to the forward direction the kinematics are such that

$$E_\nu = \frac{m_\pi^2 - m_\mu^2}{m_\pi^2 + p_\pi^2 \theta_\nu^2} p_\pi.$$

Thus for $\theta_\nu = 0$, $E_\nu = 0.42 p_\pi$, while at the maximum angle for neutrinos in the detector ($\theta_\nu = 33$ mrad), the neutrino energy drops to $0.28 p_\pi$. The neutrino energy spectrum from π decay is a slightly broadened version of the pion spectrum transmitted by the horn with the energy scaled by a factor of about 0.35. The momentum of the pions at which horn transmission is most enhanced is 3 GeV/c so that on the average 30% of the pions decay before reaching the shield. The muons from pion decay will themselves decay; the ratio of muon to pion decay is about 3×10^{-3} . The ν_e and $\bar{\nu}_\mu$ from positive muon decays have a spectrum similar to that of the ν_μ from the pion decay but with a mean energy lowered by about a factor of 2.

Kaons contribute to the spectrum primarily through the $K \rightarrow \mu \nu_\mu$ decay mode. The kinematics are similar to two-body pion decay except that the forward neutrinos have an energy very close to the parent kaon momentum throughout the angular range of the detector. The decay mode $K^+ \rightarrow \pi^0 e^+ \nu_e$ gives ν_e directly with a relative branching ratio of 0.05. The ν_e from this mode extend in energy to the maximum energy of the ν_μ from $K \rightarrow \mu \nu_\mu$, and have an average energy about $\frac{1}{3}$ of the K energy. The production rate of K^+ is about 0.05 of π^+ and the ratio of the decay lengths for pions and kaons is 6.4. These factors combine to give an expected ν_e/ν_μ ratio from K^+ and π^+ decays of approximately 7×10^{-3} integrated over all neutrino energy. The contribution of other hadrons to the ν_μ spectrum is small. In the case of ν_e , there is a measurable contribution from K_L^0 decay.

To obtain a predominantly neutrino (antineutrino) beam, the magnetic horn system is used to focus positive

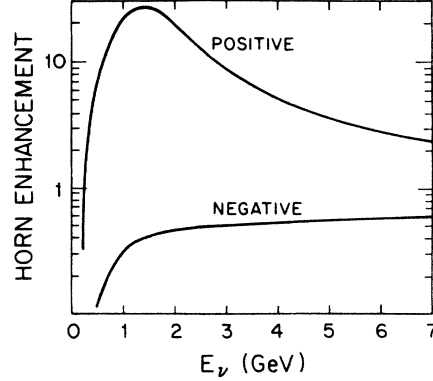


FIG. 6. Plot of the ratio of the yield of neutrinos with the horn current on to that with the horn current off. The same ratio is also shown for the opposite polarity particles.

(negative) mesons while defocusing mesons of opposite charge. In addition to enhancing the ratio of ν_μ to $\bar{\nu}_\mu$, positive focusing also increases the flux of neutrinos in the forward direction. In Fig. 6 is shown the increase in the ν_μ flux produced by the horn system relative to a bare target of the same size. The figure shows a broad enhancement due to particles of focused polarity centered at 1.3 GeV. At low momenta the mesons are over focused and strike the walls of the enclosure before they can decay. At higher momenta the enhancement is reduced because of the increasing meson decay length. Also in Fig. 6 is shown the effect of the horn system on the defocused mesons. At high neutrino energy, the effect ultimately disappears because the bending of the higher-energy mesons by the horns becomes negligible.

The ratio of the π^+ to π^- production rate is approximately two at AGS energies, and consequently the contamination of ν_μ in the primarily $\bar{\nu}_\mu$ beam is expected to be about four times that of the $\bar{\nu}_\mu$ in the ν_μ beams. It is possible to calculate the neutrino spectrum from the focused particles accurately but the opposite helicity component is generally larger than that expected from the target directly. Background processes (e.g., interactions in material downstream from the target) are likely to suffer less sign selection than direct production from the target since they traverse less of the magnetic field of the horns. The rejection of opposite helicity particles is therefore less effective. Since it is difficult to model the background processes properly, it is important to measure the yields of muons of both signs for each horn polarity during the course of an experiment.

IV. DETECTOR

The detector is shown schematically in Fig. 7. It consists of two major components: a liquid-scintillator target-detector and a proportional drift tube system which is used for particle tracking. The main detector consists of 112 modules. The total mass is 170 tons of which 100 tons are fiducial mass. More than 80% of the mass is liquid scintillator. Behind the main detector is a shower counter which consists of 10 walls of calorimeter cells

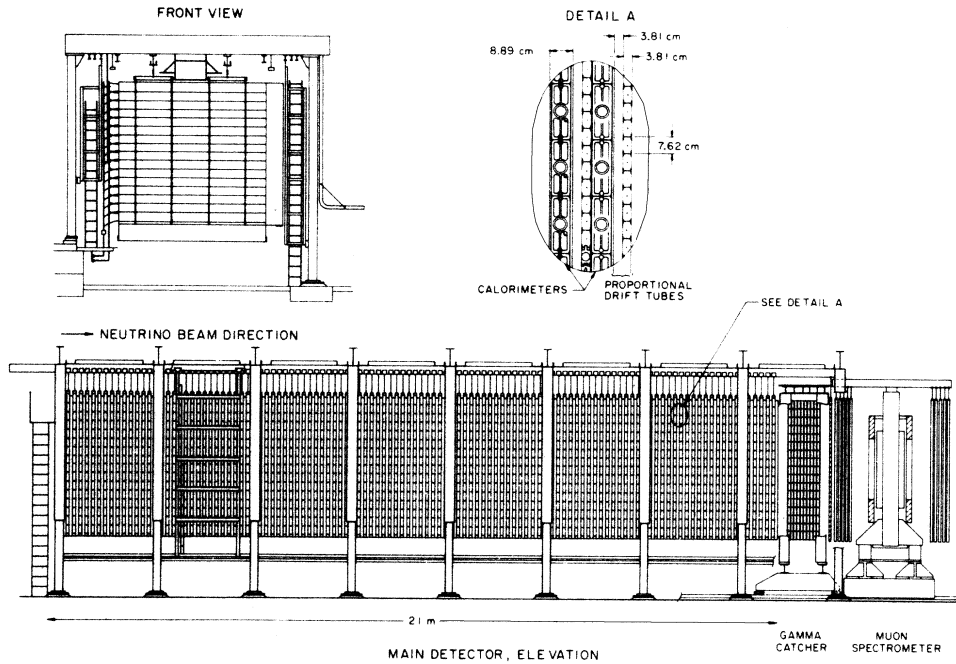


FIG. 7. A schematic drawing of the BNL-Brown-KEK-Osaka-Pennsylvania-Stony Brook neutrino detector.

with a radiation length of lead after each wall. This device is sufficiently thick to contain electromagnetic showers that originate near the end of the main detector. Behind the main detector and shower counter is a magnetic spectrometer to measure the momentum of muons produced by neutrino interactions in the main detector.

The calorimeter scintillator cells are assembled in a wall to form an area of $4.22 \text{ m} \times 4.09 \text{ m}$ with a total mass of 1.35 metric tons. Between these target planes are pairs of proportional-drift-tube (PDT) planes for particle tracking. Each pair provides an x and a y measurement of the particle position by recording the drift time in the cell. The PDT planes have an active area of $4.2 \text{ m} \times 4.2 \text{ m}$. A module of one scintillator wall and two PDT planes provides timing to 1.7 ns from the scintillator, and position to about 1.3 mm from the PDT. The pulse height is recorded from each end of a scintillator cell and for every PDT cell. For tracks which stop in the detector, energy deposition in the scintillator and PDT is used for particle identification. For showering particles the total energy is determined from the total energy deposition in the scintillator.

The calorimeter cells are extruded acrylic tubes of internal area 7.9 cm along the beam direction and 25 cm high. The walls are 3 mm thick, and light is totally internally reflected at the outside surface and transmitted to the photomultiplier tube (Amperex 2212A) at each end. The attenuation characteristics of the cells are evaluated using muons produced by the neutrino beam and are monitored frequently with cosmic rays. The response of the cells was studied extensively in a test beam.

The proportional drift tubes have 54 sense wires in each plane, each enclosed in an individual cell $3.8 \text{ cm} \times 7.6 \text{ cm} \times 4.2 \text{ m}$ long. P10 gas (90% Ar, 10% methane) is

used. The drift time measurement from these tubes yields a position accurate to 1.3 mm without substantial correction. The angular resolution is dominated by multiple scattering at the relevant particle energies. Gain stabilization is accomplished with a PDT cell of the same geometry as the cells in the main detector which is illuminated with a ^{109}Cd x-ray source.

The magnetic spectrometer utilized an air gap magnet with an aperture $1.8 \text{ m} \times 1.8 \text{ m} \times 0.46 \text{ m}$. The integrated field corresponded to an imparted transverse momentum of $40 \text{ MeV}/c$ at the center and $70 \text{ MeV}/c$ at the edge. Particle tracks in the spectrometer are defined by nine pairs of PDT planes identical to those in the main detector, arranged four before the magnet and five behind. The start time for the drift measurement is generated from the last six calorimeter walls of the main detector. Tracks are fit to a parabola in the field, and momentum is determined using the appropriate field integral and bend angle. The momentum resolution is limited by the PDT position accuracy of 1.3 mm. The momentum resolution of the spectrometer is

$$\frac{\Delta p}{p} = [0.010 + (0.067p)^2]^{1/2} \quad \text{with } p \text{ in } \text{GeV}/c.$$

V. MEASUREMENT OF THE NEUTRINO SPECTRA

Data were collected during two time periods: in the first, data were acquired from 0.89×10^{19} and 0.89×10^{19} protons incident on target (POT) for neutrinos and antineutrinos, respectively; in the second, 1.73×10^{19} and 2.62×10^{19} protons impinged on the target for neutrinos and antineutrinos, respectively. The spectrum shapes of the dominant neutrino types were essentially constant be-

tween the two data sets. There was a change in the value of the ratio $\phi(\nu_\mu)/\phi(\bar{\nu}_\mu)$, i.e., the relative ν_μ contamination in the $\bar{\nu}_\mu$ beam, which is discussed below under single-track events.

To find the neutrino spectra from the observed quasi-elastic events it is necessary to know the differential cross sections for quasielastic scattering. The dependence of the cross sections on momentum transfer (Q^2) is parametrized by dipole form factors with a vector mass M_V and an axial-vector mass M_A . The production cross section at low Q^2 must be modified for the effects of the Pauli exclusion principle, and the apparent momentum transfer must be modified for the Fermi motion of the struck nucleon.⁷ Fermi motion limits the resolution on the neutrino energy when calculated from the observed muon angle and momentum to about 15% full width at half maximum (FWHM) for the kinematic range in this experiment. A detailed Monte Carlo calculation was employed which includes these effects, as well as apparatus resolution, to determine the acceptance of the apparatus as a function of E_ν and Q^2 .

Two data samples were used to reconstruct the neutrino energy. They are distinguished by event topology: (i) one track originating in the detector or (ii) two tracks emanating from a common vertex in the detector. Two-track events are available only in the ν_μ (and ν_e) data samples. Before a track can be reconstructed in the detector it must traverse at least three detector modules. For $\nu_\mu n \rightarrow \mu^- p$ events this implies that the recoil proton may be reconstructed only if the momentum transfer $Q^2 > 0.3$ (GeV/c)². Hence events with $Q^2 < 0.3$ (GeV/c)² exhibit single-track topology. The backgrounds for both event types are largely due to charged current single-pion production. When the neutrino energy is inferred from the muon angle and momentum alone, the measured neutrino energy distribution is in agreement with that deduced from two-track events.

A. Single-track events

Single-track events are classified in two ways: events in which the muon stops in the detector, and events in which the muon leaves the detector and traverses the muon spectrometer.

When the muon originates in the fiducial volume and stops in the body of the detector the range may be measured and the energy calculated. To reduce hadronic contamination these muons are required to traverse more than 15 modules without significant scattering. The selection limits the acceptance to neutrinos above 300 MeV, but since both the flux and cross section are small below this energy, the limit is not important. The upper energy limit is given by the overall length of the detector and is about 1.5 GeV. There were 2284 and 2665 events in the neutrino and antineutrino data sets, respectively. Background levels from pion production were $(39 \pm 8)\%$ and $(31 \pm 6)\%$, respectively.

Muons which traverse the muon spectrometer are analyzed in a similar way. The muon energy is determined from the momentum measured in the magnet plus the calculated energy loss in the detector. The aperture of

the magnet and the position relative to the main detector limited the acceptance to neutrinos above 0.8 GeV. An upper limit of 5 GeV was chosen to guarantee good momentum resolution and accurate sign selection. Totals of 5112 μ^- and 179 μ^+ events were obtained during the second neutrino run, and 2883 (2551) μ^+ and 313 (391) μ^- events were collected during the first (second) antineutrino run. Inelastic background levels in these samples were estimated to be $(18 \pm 3)\%$ for μ^- and $(13 \pm 3)\%$ for μ^+ events after limits were placed on the energy deposited at the origin of the tracks. The contamination of antineutrinos in the neutrino data set was determined to be 0.024 ± 0.005 . The corresponding results for neutrino contamination in the antineutrino beam were 0.051 ± 0.008 for the first sample and 0.087 ± 0.013 for the second sample. The difference in these latter values is attributed to variations in targeting efficiency which gave rise to an enhanced contribution in the second run from pions that were defocused by the horn system. This observation emphasizes the importance of direct measurement by a muon spectrometer of the helicity content of the incident beam in any neutrino experiment.

B. Two-track events

Events exhibiting a muon and a recoil proton sufficiently long to be reconstructed as a track were discussed in Ref. 3. It is required that the proton stop in the detector so that the energy may be determined from the range. The stopped track is identified as a proton by the pattern of deposited energies in the scintillator cells and the PDT (Ref. 2). The proton length requirement limits the acceptance to events with neutrino energy above 500 MeV; the acceptance is roughly constant above that energy. There were 4889 events in the neutrino data set with a $(24 \pm 5)\%$ background.

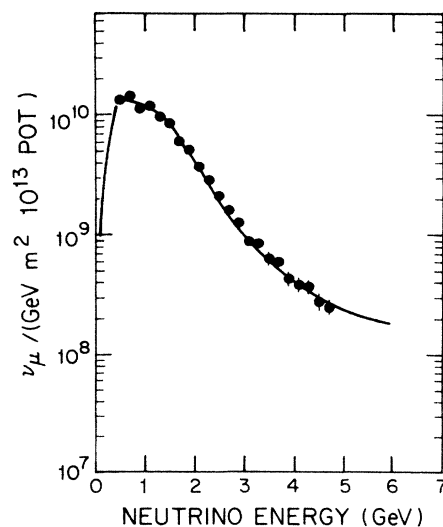


FIG. 8. The measured flux $\phi(E(\nu_\mu))$ together with the calculated result of Fig. 12. The data have been adjusted by a factor of 1.1 consistent with the scale uncertainties in the data and Monte Carlo calculations. POT stands for protons incident on target.

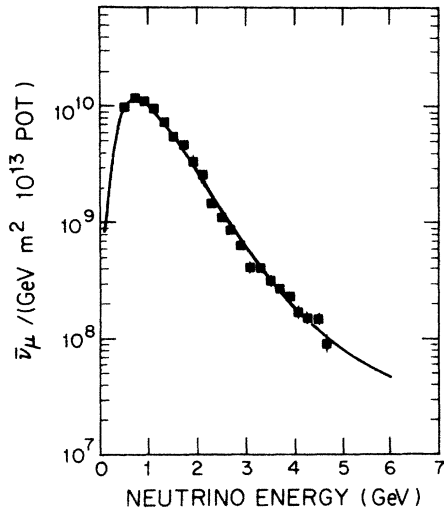


FIG. 9. The measured flux $\phi(E(\bar{\nu}_\mu))$ together with the calculated result of Fig. 13. The data have been adjusted by a factor of 1.3 consistent with the scale uncertainties in the data and Monte Carlo calculations.

C. Results

The neutrino fluxes $\phi(E(\nu_\mu))$ and $\phi(E(\bar{\nu}_\mu))$ derived from the combined stopping, spectrometer, and two-track event data sets are shown in Figs. 8 and 9, respectively. The flux measurements were internally consistent within an expected error of 15%.

The flux $\phi(E(\nu_e))$ is measured by means of reaction (7), $\nu_e n \rightarrow e^- p$, with electrons identified through the electromagnetic shower they produce.³ The electron energy is measured by summing the depositions in the calorimeter elements with a correction for unobserved energy. The

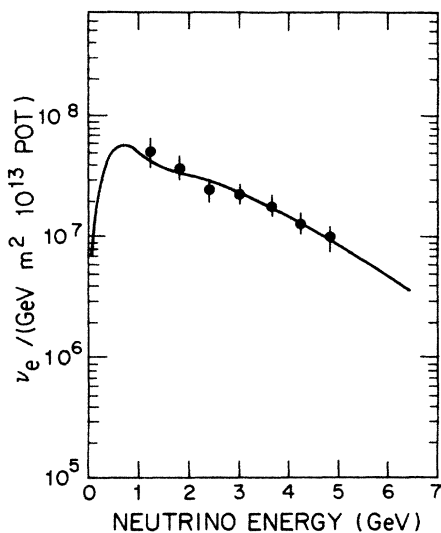


FIG. 10. The measured flux $\phi(E(\nu_e))$ together with the calculated result of Fig. 14. The data have been adjusted by a factor of 1.1 consistent with the scale uncertainties in the data and Monte Carlo calculations.

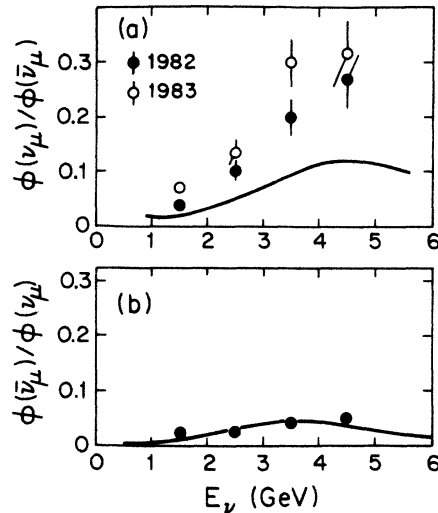


FIG. 11. The ratios (a) $\phi(E(\nu_\mu))/\phi(E(\bar{\nu}_\mu))$ and (b) $\phi(E(\bar{\nu}_\mu))/\phi(E(\nu_\mu))$ giving the fractional flux of opposite helicity neutrinos in each helicity beam. The curve is the calculated ratio in each case.

angle of the electron is measured with the earliest-hit PDT elements before substantial scattering takes place. Events are selected in which the electron angle is less than 15° . The principal background in the electromagnetic shower sample arises from photons from π^0 decay originating in a neutral-current event upstream of the shower vertex. This photon background is identified by its different energy distribution and is subtracted from the electron sample. Extraction of the ν_e flux is discussed in detail in Ref. 3. The measured flux $\phi(E(\nu_e))$ is shown in Fig. 10.

Figure 11 shows the spectrum of opposite-helicity neutrinos in a given helicity beam derived from events in the spectrometer. The “contamination” ratios $\phi(\bar{\nu}_\mu)/\phi(\nu_\mu)$ and $\phi(\nu_\mu)/\phi(\bar{\nu}_\mu)$ increase with neutrino energy because the effect of horn focusing is reduced with increasing parent pion energy.

VI. BEAM CALCULATION

The neutrino spectra have been calculated by a Monte Carlo method using a program from the CERN HYDRA Applications Library described by Visser. The program NUBEAM has been adapted by Carlini to run on the VAX 11/780 (Ref. 8). The program generates particles according to a production spectrum, and traces the selected particle through the beam elements until a decay occurs or the particle is absorbed. When a decay occurs, the particles which are products of this decay are themselves propagated until the decay chain is exhausted or the particles are absorbed in the shield. A single secondary particle decay will create a series of daughter particles of appropriate weight, including all species of neutrino. The weights are modified to include the effects of absorption as well as multiple scattering in the case of the muons. The sum of properly normalized probabilities for all the particles involved gives the neutrino flux at the detector.

TABLE I. Collision lengths in gm/cm².

	Be	C	Al	Fe	Sapphire
p	75.2	86.3	106.4	131.9	97.1
π	102.5	113.4	134.3	160.7	123.0
K^-	113.5	124.4	145.5	172.9	132.8
K^+	117.0	127.7	155.4	187.2	141.8

Input data to the program fall under the following headings: (i) particle properties, (ii) beam geometry, (iii) material properties including interaction cross sections, and (iv) particle-production rates.

(i) *Particle properties.* These are the decay modes and branching ratios of the secondary particles and their cross sections for absorption on nuclei.⁹

(ii) *Beam geometry.* The beam geometry is assumed to be cylindrically symmetric and is derived from the surveyed locations of the beam elements and their internal structure. The magnetic field of the horn is calculated from a current sheet specified by the horn geometry.

(iii) *Material properties.* The proton target is more than an interaction length long, and the attenuation of the proton beam in the target is important. In the energy range of this experiment, and for the aspect ratio of the proton target, most of the elastically scattered protons remain within the target. Scattering processes in which the momentum transfer is small leave the proton able to produce more secondary particles. The program uses a single exponential for the proton beam attenuation with a single effective collision length that models the behavior of the protons. In Table I are shown the collision lengths that were used. A similar but lesser problem exists with the secondary mesons when they traverse the material of the horns. Again, a single effective interaction length is chosen that models the secondary beam loss.⁹

(iv) *Particle-production rates.* Particle-production rates

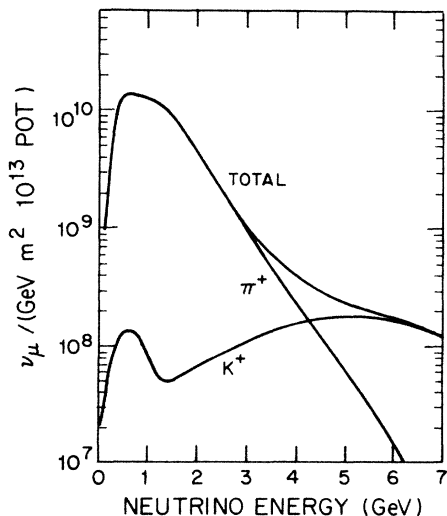


FIG. 12. The calculated flux $\phi(E(\nu_\mu))$ with the component contributions also shown.

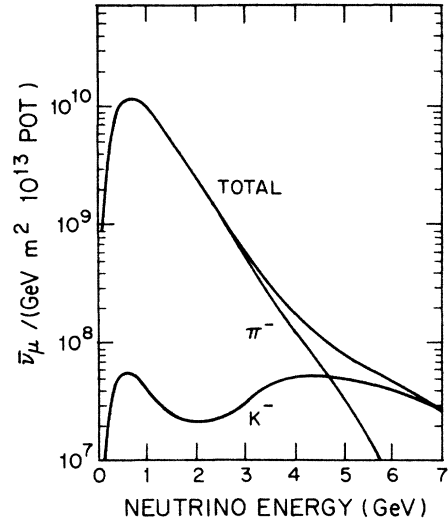


FIG. 13. The calculated flux $\phi(E(\bar{\nu}_\mu))$ with the component contributions also shown.

at proton energies near 30 GeV have been measured and fit to empirical formulas by Sanford and Wang¹⁰ and Grote, Hagedorn, and Ranft (GHR) (Ref. 11). The beam calculations described here were based on the GHR parametrization; that of Sanford and Wang was used for comparison. An estimate was made of pion production by reinteracting protons guided by the shape of the observed ν_μ spectrum and the observed angular distribution of muons from quasielastic events. The procedure is described¹² in the Appendix. Briefly, it amounts to modification of the lowest pion momentum bins in the momentum-angle matrix of GHR that describes pion production. A small adjustment of the integrated K^+/π^+ ratio (increased by a factor of 1.25) is also made, con-

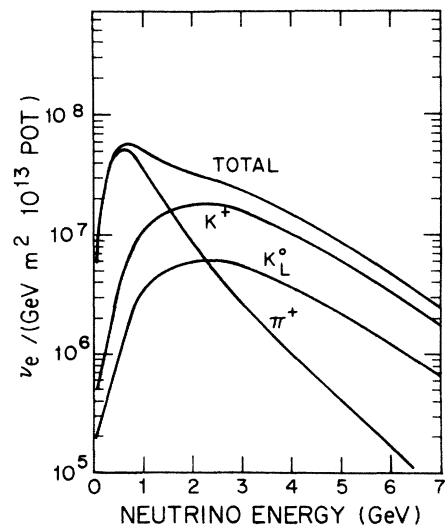


FIG. 14. The calculated flux $\phi(E(\nu_e))$ with the component contributions also shown.

sistent with the stated uncertainty on that quantity in Refs. 10 and 11. The yield of charged pion and kaon beams at the AGS (Ref. 13) served to check the secondary meson production data.

The results of the calculations of the total fluxes $\phi(E(\nu_\mu))$, $\phi(E(\bar{\nu}_\mu))$, $\phi(E(\nu_e))$, and $\phi(E(\bar{\nu}_e))$ are shown in Figs. 12–15, which also show the contributions from the different meson (and muon) decays. The total fluxes $\phi(E(\nu_\mu))$, $\phi(E(\bar{\nu}_\mu))$, and $\phi(E(\nu_e))$, are shown again in Figs. 8–10 for comparison with the measured fluxes. The shapes of the calculated fluxes are in good agreement with those of the measured fluxes. To obtain the agreement shown on the vertical scale, the ν_μ and ν_e data were adjusted by the factor 1.1, and the $\bar{\nu}_\mu$ data by the factor 1.3.

The results of the calculations of the ratios $\phi(E(\nu_\mu))/\phi(E(\bar{\nu}_\mu))$ and $\phi(E(\bar{\nu}_\mu))/\phi(E(\nu_\mu))$ are shown in Fig. 11 for comparison with the measured values of the opposite helicity contaminations in the primarily $\bar{\nu}_\mu$ and primarily ν_μ beams. The calculation of $\phi(E(\bar{\nu}_\mu))/\phi(E(\nu_\mu))$ fits the data quite well except perhaps at the lowest energy point. The calculation of $\phi(E(\nu_\mu))/\phi(E(\bar{\nu}_\mu))$ is significantly below the data. When negative mesons are focused by the horn system positive mesons are defocused and interact in the material of the horns. This interaction is not taken into account in the calculation. The effect is more important for negative charge focus because of the larger production cross sections for positive mesons. The disagreement between the measured and calculated values of $\phi(E(\nu_\mu))/\phi(E(\bar{\nu}_\mu))$ stresses again the need for direct measurement of the opposite helicity contamination in a neutrino beam employed in an experiment.

Another significant result of the flux calculation is the prediction of the radial dependence of the neutrino energy distribution in a horn focused neutrino beam. This is exhibited in Fig. 16 which shows the ratio of the flux in a 2.5-m \times 2.5-m cross-sectional area averaged over a given length of the detector to the flux in a 3.0-m \times 3.0-m

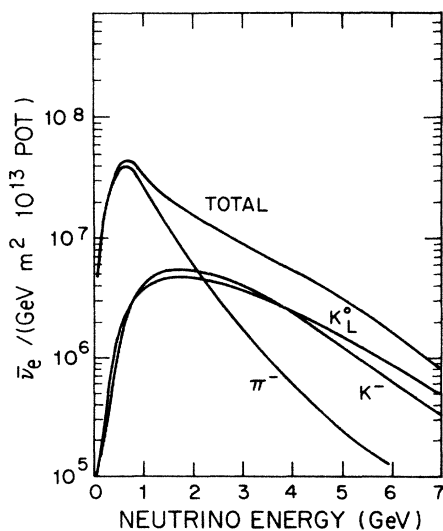


FIG. 15. The calculated flux $\phi(E(\bar{\nu}_e))$ with the component contributions also shown.

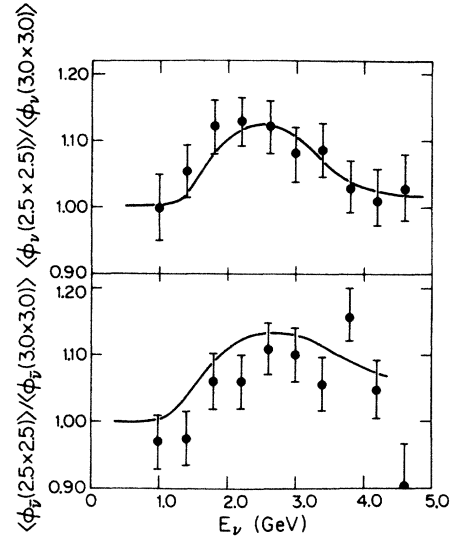


FIG. 16. Plots showing the radial dependence of the neutrino energy distributions for (a) ν_μ and (b) $\bar{\nu}_\mu$.

cross-sectional area averaged in the same way. The calculated result is compared with data obtained from single-track events that traverse the magnetic spectrometer. One sees that the relative number of neutrinos with energies between about 2 and 4 GeV is 10% greater in the smaller area than in the larger area. This holds for both ν_μ and $\bar{\nu}_\mu$ beams, and is confirmed by the measurements.

The agreement of data and calculation in Figs. 8–10 and 16 follows from relatively minor modification of the thin target yield of low-momentum pions from proton-nucleus collisions at 28.3 GeV, which takes into account the thick target employed in neutrino-beam production. We emphasize that a single modification (described in the Appendix) leads to the calculated neutrino fluxes and the agreement exhibited. In view of the success of this calculation in reproducing the wide-band neutrino spectra of ν_μ , $\bar{\nu}_\mu$, and ν_e , it seems likely that a similar calculation may be used to predict accurately neutrino fluxes generated under different conditions, e.g., bare-target and narrow-band beams.

ACKNOWLEDGMENTS

It is a pleasure to acknowledge the fruitful collaboration with R. Carlini in the understanding of the program NUBEAM. We wish to thank R. R. Rau and N. P. Samios of the Brookhaven National Laboratory for their encouragement and the staff of the AGS at the Brookhaven Physics Department for their cooperation. We also wish to thank the technical assistance personnel at the respective universities for their excellent and untiring support. This work was supported in part by the U.S. Department of Energy and the Japanese Ministry of Education, Science and Culture through the Japan-U.S.A. Cooperative Research Project on High Energy Physics.

APPENDIX

The flux program NUBEAM was modified to account for the fact that the GHR compendium is for thin-target production, and NUBEAM does not model secondary interactions. Shown in Table II as an example is the GHR positive-pion production spectrum in the form of an 18×18 matrix in θ_π and p_π . Secondary interactions mainly of the protons degrade the production spectrum primarily in momentum and leave the angle spectrum rel-

atively untouched. To modify the production spectrum to fit the neutrino data we multiplied the four p_π columns (1, 2, 3, 4 GeV/c) by four parameters which alter the neutrino flux spectrum only below 1.2 GeV. The fit parameters are relatively small (1.18, 1.79, 1.24, 1.21 in increasing order of p_π) and the modification is consistent with the effect expected from secondary interactions. We have calculated $\phi(E(\bar{\nu}_\mu))$, $\phi(E(\nu_e))$, and $\phi(E(\bar{\nu}_e))$ using the same four parameters.

*Deceased.

†Permanent address: Singer Co., Kearfott Div., Wayne, NJ 07470.

‡Present address: National Laboratory for High Energy Physics (REK), Tsukuba-gun, Ibaraki-ken, Japan.

§Permanent address: Christopher Newport College, Dept. of Physics, Newport News, VA 23606

**Permanent address: Cornell University, Dept. of Physics, Ithaca, NY 14853

¹L. A. Ahrens *et al.*, Phys. Rev. Lett. **51**, 1514 (1983); **54**, 18 (1985).

²K. Abe *et al.*, Phys. Rev. Lett. **56**, 1107 (1986).

³L. A. Ahrens *et al.*, Phys. Rev. D **31**, 2732 (1985).

⁴N. Baker *et al.*, Phys. Rev. D **23**, 2499 (1981); K. L. Miller *et al.*, *ibid.* **26**, 537 (1982); T. Kitagaki *et al.*, *ibid.* **28**, 436 (1983).

⁵W. T. Weng, IEEE Trans. Nucl. Sci. **NS-30**, 2956 (1983); W. T. Weng *et al.*, BNL Report No. 51310, 1979 (unpublished).

⁶The literature on neutrino beams and magnetic-horn design is sparse. A high-intensity neutrino beam was described in M. Giesch *et al.*, Nucl. Instrum. Methods **20**, 58 (1963), where an estimate of the expected neutrino flux was made. The neutrino beam at the Brookhaven AGS has used a horn geometry which was initially described in R. Palmer, *Proceedings of an Informal Conference on Experimental Neutrino Physics*,

CERN, 1965, edited by C. Franzinetti (CERN Report No. 65-32, 1965).

⁷A detailed presentation of the quasielastic cross sections can be found in C. H. Llewellyn Smith, Phys. Rep. **3C**, 262 (1972). The vector and axial-vector masses used by us were $M_V=0.84$ GeV and $M_A=1.03$ GeV. Corrections for Pauli exclusion and Fermi momentum are treated in J. S. Bell and C. H. Llewellyn Smith, Nucl. Phys. **B28**, 317 (1971); J. Mougey *et al.*, Nucl. Phys. **A262**, 461 (1976).

⁸C. Visser, NUBEAM, a neutrino-beam simulator, Hydra Applications Library, CERN, 1979. This program was modified extensively by R. Carlini, Los Alamos National Laboratory. The program and input data appropriate for a 28-GeV proton beam may be obtained from D. H. White, Physics Department, Brookhaven National Laboratory, Upton, New York 11973.

⁹Particle Data Group, Rev. Mod. Phys. **56**, S1 (1984); A. S. Carroll *et al.*, Phys. Lett. **80B**, 319 (1979).

¹⁰J. R. Sanford and C. L. Wang, BNL Report No. 11479, 1967 (unpublished).

¹¹H. Grote, R. Hagedorn, and J. Ranft, CERN report, 1970 (unpublished).

¹²D. H. White, BNL Report No. 36278, OG 793, 1985 (unpublished).

¹³G. Bunce, BNL Report No. 50874, 1978 (unpublished).